



Nickel cobalt hydroxide nanoflakes as catalysts for the hydrogen evolution reaction

Stève Baranton, Christophe Coutanceau*

Université de Poitiers, IC2MP, Laboratoire "Catalyse et Milieux non conventionnels" UMR CNRS 7285, 4 rue Michel Brunet, 86022 Poitiers Cedex, France



ARTICLE INFO

Article history:

Received 2 October 2012

Received in revised form 16 January 2013

Accepted 21 January 2013

Available online 9 February 2013

Keywords:

Alkaline medium

Alloys

Cobalt

Hydrogen evolution reaction

Nickel

ABSTRACT

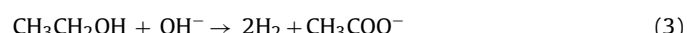
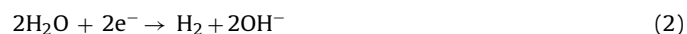
The activity of $\text{Ni}_x\text{Co}_{10-x}/\text{C}$ catalysts for the hydrogen evolution reaction (HER) was evaluated. The $\text{Ni}_x\text{Co}_{10-x}/\text{C}$ ($0 \leq x \leq 10$) nano-catalysts were synthesized by a water-in-oil microemulsion method and were then characterized by thermogravimetric analysis (TGA), transmission electron microscopy (TEM) and X-ray diffraction (XRD). The control of a metal loading of ca. 30 wt% on carbon was confirmed for all catalysts from TGA, while TEM images and XRD patterns revealed the formation of nickel cobalt hydroxide nano-flakes with a preferential growth along the (100) and (010) directions. The electrochemical investigations in 0.1 M NaOH confirmed the interaction between nickel and cobalt in the catalytic materials, and their activity towards the HER. The catalytic activity increased regularly with the increase of the cobalt content in the $\text{Ni}_x\text{Co}_{10-x}/\text{C}$ materials. The short term stability measurements performed by chronoamperometry revealed that dissolution of cobalt occurred. Hence, amongst the nickel cobalt hydroxides synthesized, $\text{Ni}_5\text{Co}_5/\text{C}$ and $\text{Ni}_7\text{Co}_3/\text{C}$ catalysts were found to present a good compromise between catalytic activity for the HER and stability.

© 2013 Elsevier B.V. All rights reserved.

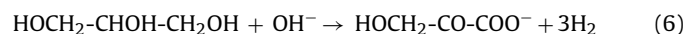
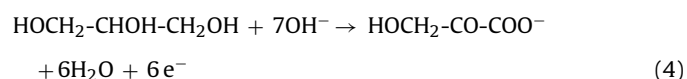
1. Introduction

Hydrogen is an interesting energy carrier which could strongly limit the greenhouse gas emissions, depending on the energy source used for its production. Using renewable energy sources, such as hydroelectric power, wind, solar and tidal power, or low carbon emission source such as nuclear power, the production of hydrogen by water electrolysis is the most developed process, leading to high purity hydrogen, suitable to feed a low temperature fuel cell, such as a PEMFC or an AFC [1]. However, due to high overvoltages required to perform water electrolysis, particularly for the activation of the oxygen evolution reaction at the anode, the electrochemical hydrogen production cost is not competitive when compared with other production processes from natural gas (auto thermal reforming, methane steam reforming, partial oxidation). The working voltage of a water electrolysis cell is indeed close to 2.0 V leading to high energy consumption for hydrogen production (reaching more than 50 kWh kg⁻¹ (the theoretical value under standard conditions being 33 kWh kg⁻¹). In order to save energy, the use of alcohols in electrolysis cells was recently investigated, leading to the formation of hydrogen and reaction products from the alcohol oxidation [2,3]. Eqs. (1)–(3) are an example of this

alcohol electrolysis process in the case of ethanol oxidation into acetate in alkaline medium:



Such process presents a very low thermodynamic voltage (lower than 0.1 V for most of alcohols) due to oxidation potentials of alcohols in the range from 0 V to 0.2 V vs. RHE [4]. Furthermore, the use of an alcohol issued from biomass or a by-product from another process with a low environmental factor [5], such as glycerol for example [6], allows keeping a low environmental impact for the hydrogen production process from alcohol electrolysis. Hence, it is possible through the electrochemical valorization of an alcohol into value added chemicals (for example hydroxypyruvate ion) to obtain high purity hydrogen with a low working voltage for the electrolysis cell when compared to water electrolysis as illustrated in Fig. 1a and Eqs. (4)–(6).



* Corresponding author. Tel.: +33 5 49 45 48 95.

E-mail address: christophe.coutanceau@univ-poitiers.fr (C. Coutanceau).

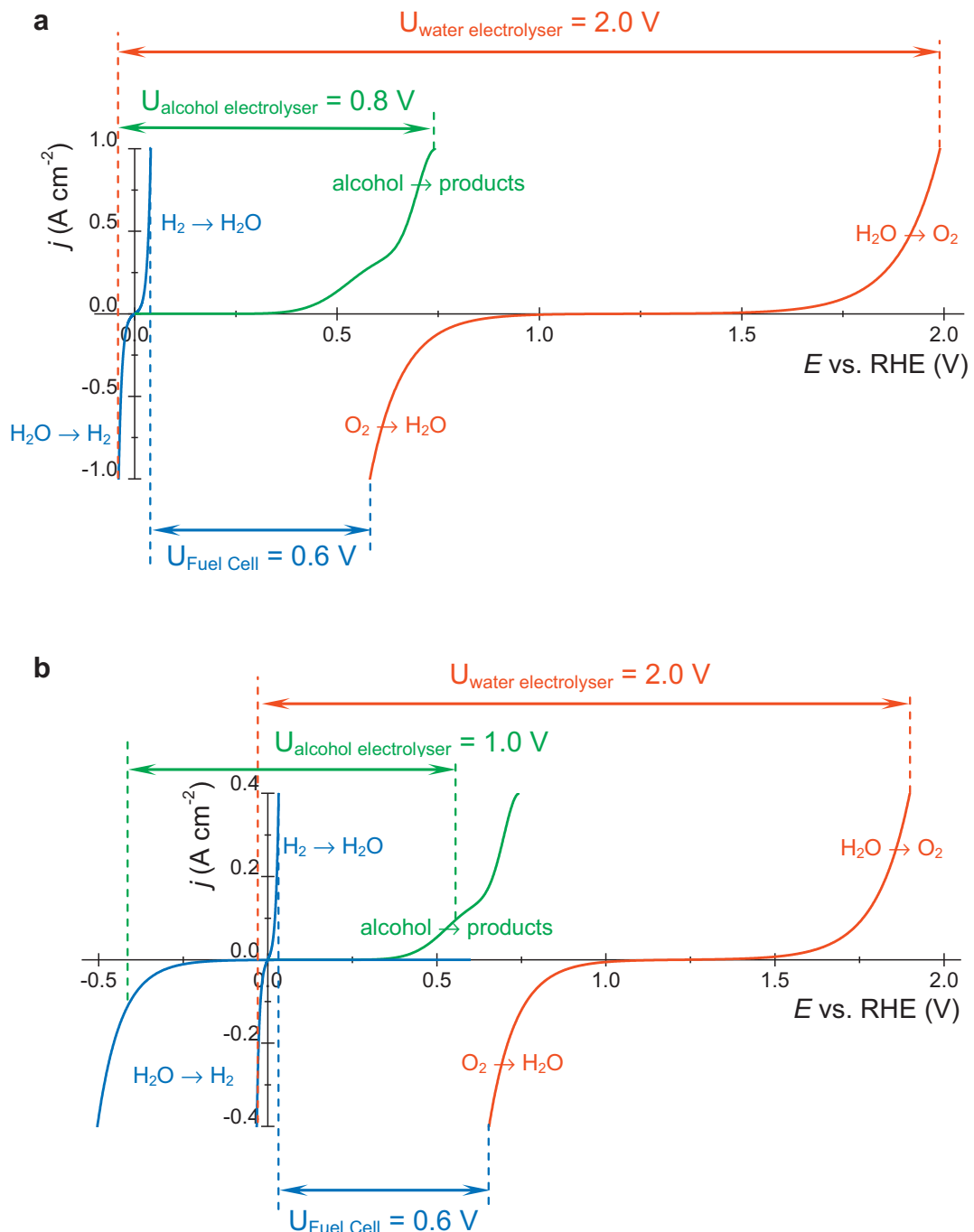


Fig. 1. Comparison of the theoretical $E(j)$ electric characteristics representative of the Butler–Volmer kinetics law for water oxidation, alcohol oxidation, oxygen reduction and proton reduction. ($U_{\text{fuel cell}}$) is the cell voltage for hydrogen/oxygen fuel cell at a current density of 1 A cm^{-2} ; ($U_{\text{water electrolyzer}}$) and ($U_{\text{alcohol electrolyzer}}$) are the cell voltages for water electrolysis and alcohol electrolysis at a current density of (a) 1 A cm^{-2} and (b) 0.1 A cm^{-2} .

Considering the higher reactivity of alcohols in alkaline medium than in acidic medium, anode materials for the oxidation of alcohols in alkaline medium were developed with low platinum content [7,8] or without platinum [9–11]. Hence, the implementation of alcohol electrolysis for the production of value added chemicals and hydrogen could be considered in alkaline medium, with alkaline membranes [12,13] or in alkaline aqueous medium with a porous separator. However, the selectivity of most anode materials investigated depends on the potential range considered [7], and in most case, the electrolysis of organic products does not allow current densities higher than a few hundreds mA cm^{-2} [12,14].

A significant production of hydrogen could then only be achieved with a high surface of electrodes. Under these conditions, despite the high activity of this material for the hydrogen evolution reaction (HER), a platinum based cathode would represent an expensive material, limiting the interest of this process for hydrogen production.

It is then proposed in the present work to investigate the electrochemical behavior of alternative cathode materials based on transition metals for the HER in alkaline medium. Considering that platinum presents a high activity for the HER, the use of transition metals as cathode material may change the concept described

in Fig. 1a into a process working at higher voltage (Fig. 1b). However, an increase of the alcohol electrolysis voltage up to 1 V as presented in Fig. 1b would still represent a 60% electrical yield between the production of hydrogen at 1 V and its consumption as a fuel in a PEMFC working at 0.6 V. Of course, this yield does not take into account the consumption of alcohol (which impact on the global process can be reduced by the use of a by-product of another process, such as glycerol) or the production of value added chemicals. Furthermore, the use of non noble metals as cathode material, presenting a low activity for alcohol oxidation reaction, could avoid the alcohol tolerance issue of platinum based catalysts. Indeed, if the potential domain considered for HER may not allow alcohol oxidation even on platinum based materials, and consequently, may not lead to a depolarization of the cathode, the platinum surface can adsorb alcohols with the formation of CO at very low potential [7,9,15]. The presence of alcohol in the reaction medium of the hydrogen cathode could then lead to a poisoning of a platinum based cathode. While not investigated in the present work, the tolerance to a surface poisoning of a transition metal based cathode for the HER due to the presence of alcohol is likely to be higher than that of platinum.

The present work describes the synthesis, the characterization and the electrochemical study of nickel cobalt alloy nanoparticles dispersed on a carbon substrate for the hydrogen evolution reaction. Nickel and cobalt were the transition metal chosen for their stability and their activity for various electrochemical reactions in alkaline medium [16–18]. Furthermore, the low cost of these transition metals compared to classically used catalysts for the HER makes them suitable for high surface cathode working at low current density.

2. Experimental

2.1. Nickel cobalt catalyst preparation

The nickel cobalt alloys were synthesized by a water-in-oil microemulsion method and the resulting materials are called $\text{Ni}_x\text{Co}_{10-x}/\text{C}$ with $0 \leq x \leq 10$. The control of the atomic ratio x is performed a priori by using the corresponding molar ratios of metal salts in the synthesis. Table 1 summarizes the different $\text{Ni}_x\text{Co}_{10-x}/\text{C}$ catalysts synthesized. Briefly, the water-in-oil synthesis method involves the dissolution of nickel sulfate and cobalt sulfate ($\text{NiSO}_4 \cdot 6\text{H}_2\text{O}$ and $\text{CoSO}_4 \cdot 7\text{H}_2\text{O}$, 99% from Sigma Aldrich) in ultrapure water (MilliQ®, Millipore 18.2 MΩ cm) to obtain a metal concentration of 0.2 mol L^{-1} (concentration of nickel + cobalt ions in solution). A microemulsion was obtained by mixing 1.6 mL of the aqueous solution with 34.26 g of n-heptan (VWR, HPLC grade) and 19.02 g of Brij® 30 amphiphilic surfactant (Sigma–Aldrich). Solid NaBH_4 was then added in large excess to the mixture (350 mg)

and after one hour, a given amount of carbon (Vulcan XC 72, Cabot corp.) was added in order to reach a 30 wt% metal loading on carbon and ultrasonically dispersed with nanoparticles for 15 min. After this dispersion step, 50 mL of acetone was added to the synthesis medium before its filtration on a nitrocellulose membrane with 0.22 μm pore diameter (Millipore). The $\text{Ni}_x\text{Co}_{10-x}/\text{C}$ catalyst was then redispersed and filtered three more times in 100 mL acetone, three times in 100 mL ethanol and finally three times in 100 mL water. Before it was used for characterization and electrochemical study, the catalyst was dried overnight in an oven at 80 °C.

2.2. Physical characterizations

Thermogravimetric analyses (TGA) were carried out using a thermobalance Q600 DTA instrument. The measurements were done by heating the samples from 25 to 900 °C or 1100 °C with a heating rate of $10^\circ\text{C min}^{-1}$ under an air flow of 100 mL min^{-1} . Atomic absorption (AA) was performed on $\text{Ni}_x\text{Co}_{10-x}/\text{C}$ catalysts after dissolution of metals in acidic solution (concentrated nitric, hydrofluoric and hydrochloric acid solution). The dissolution is performed under microwave irradiation for 2 h in sealed Teflon reactors. UV visible spectroscopy was performed on an Evolution 100 UV visible spectrophotometer from Thermo Electron Corp. Transmission electron microscopy (TEM) measurements were carried out with a JEOL JEM 2010 (HR) with a resolution of 0.35 nm. X-ray diffraction (XRD) patterns were recorded on a Bruker D 5005 Bragg-Brentano (θ - θ) diffractometer operated with a copper tube powered at 40 kV and 40 mA ($\text{CuK}\alpha_1 = 1.54060 \text{ \AA}$ and $\text{CuK}\alpha_2 = 1.54443 \text{ \AA}$). Measurements were performed from $2\theta = 30^\circ$ to $2\theta = 80^\circ$ in step mode, with steps of 0.06° and a fixed acquisition time of 10 s step^{-1} .

2.3. Electrochemical characterizations

The working electrode is prepared by deposition of a catalytic ink on a glassy carbon disk according to a method proposed by Gloagen et al. [19]. The catalytic powder (10 mg) is added to a mixture of 0.2 mL Nafion® solution (5 wt% from Aldrich) in 1 mL isopropanol (99.5% Sigma Aldrich). After ultrasonic homogenization of the catalyst/C-Nafion® ink, 3 μL were deposited from a microsyringe onto a freshly polished glassy carbon substrate yielding a catalytic powder (metal catalyst + carbon) loading of $350 \text{ \mu g cm}^{-2}$ with 22 μg of Nafion (6 wt%), leading to a catalytic layer thickness close to 1–1.5 μm [20]. The solvent was then evaporated in a stream of pure nitrogen at room temperature. The electrochemical set-up consisted in an analog Scanning Potentiostat, Model 362 from Princeton Applied Research equipped with an analog-to-digital converter for data acquisition. The electrochemical experiments were carried out at 20 °C in N_2 -purged supporting electrolyte, using a thermostated standard three-electrode electrochemical cell. The

Table 1
metal loading and composition of $\text{Ni}_x\text{Co}_{10-x}/\text{C}$ catalysts from TGA and atomic absorption.

Catalyst	Metal loading from TGA (wt%)	Content from AA (at%)			
		Fresh catalyst		After 2 h at -0.4 V	
Ni/C	25	Ni	100	Co	–
$\text{Ni}_9\text{Co}_1/\text{C}$	29	Ni	93	Co	–
$\text{Ni}_7\text{Co}_3/\text{C}$	31	Ni	75	Co	23
$\text{Ni}_5\text{Co}_5/\text{C}$	27	Ni	56	Co	31
$\text{Ni}_3\text{Co}_7/\text{C}$	31	Ni	32	Co	42
$\text{Ni}_1\text{Co}_9/\text{C}$	26	Ni	13	Co	–
Co/C	31	Ni	–	Co	100

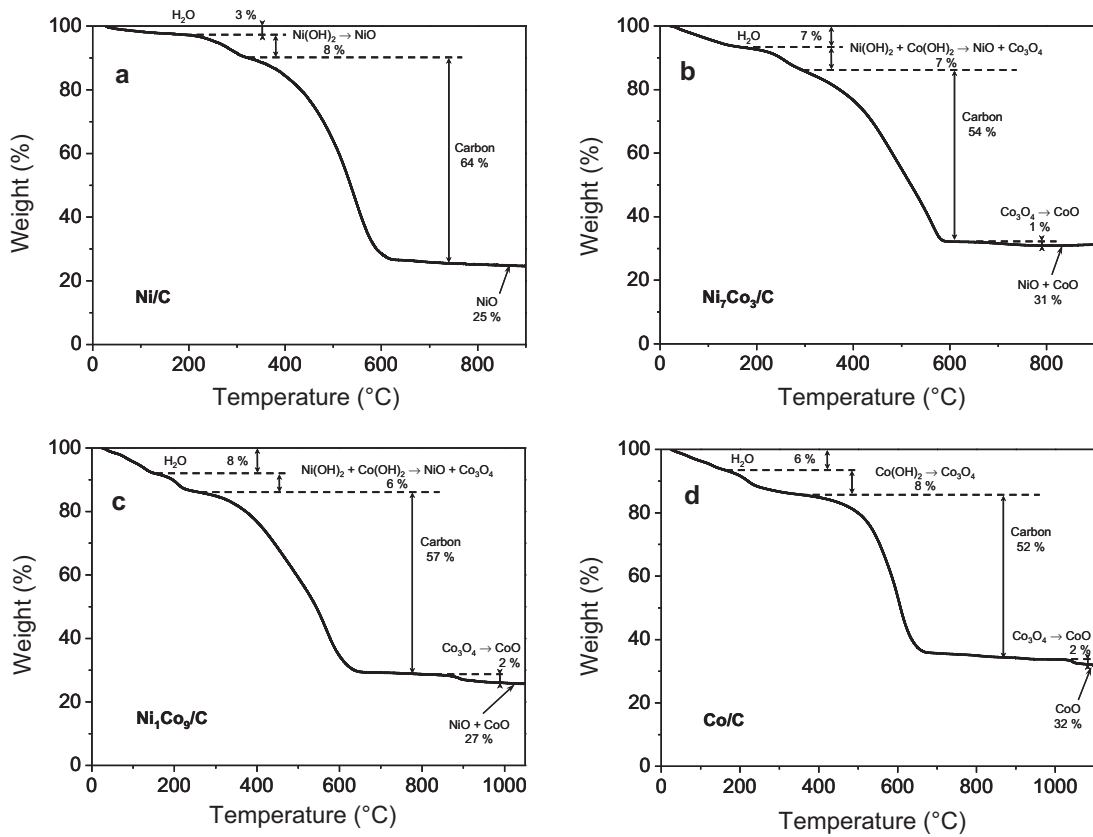


Fig. 2. Thermogravimetric analysis of (a) Ni/C, (b) Ni₇Co₃/C, (c) Ni₁Co₉/C and Co/C catalysts presented with the mass loss at each step and the associated reaction. The final oxide content is also indicated.

working electrode was a glassy carbon disk (0.071 cm² geometric surface area), the counter electrode was a glassy carbon plate (8 cm² geometric surface area) and the reference electrode was a Reversible Hydrogen Electrode (RHE). All potentials are referred to the RHE. The support electrolyte was a 0.1 M NaOH (Semiconductor Grade 99.99%, Sigma–Aldrich) solution in ultra pure water.

For short term stability measurements the catalytic inks were deposited on a 2 cm² glassy carbon working electrode. The catalytic powder loading (metal catalyst + carbon) on the 2 cm² working electrode is similar to that of experiments performed on 0.071 cm² working electrode (350 µg of catalytic powder and 22 µg of Nafion per cm²). The characterization of catalyst compositions after short term stability measurements was carried out by dissolving the Ni_{10-x}Co_x catalysts after the electrochemical experiments in a concentrated nitric and hydrochloric acid solution. The solution was then diluted before the analysis by atomic absorption.

3. Results and discussion

3.1. Physicochemical characterizations

The curves recorded during TGA performed on Ni/C, Ni₇Co₃/C, Ni₁Co₉/C and Co/C are presented in Fig. 2. The mass changes with the increase of temperature for Ni/C (Fig. 2a) reveal, after the adsorbed and intercalated water loss, a first transition due to Ni(OH)₂ dehydration and the formation of NiO between 200 °C and 300 °C. This transition is then followed by the combustion of the carbon substrate, and the remaining material corresponds to NiO. The same behavior is observed for Co/C catalyst (Fig. 2d), with a water desorption followed by the dehydration of Co(OH)₂ into Co₃O₄ between 200 °C and 300 °C [21,22] and the carbon combustion. In

the case of cobalt containing catalysts, a last mass loss corresponding to the transition from Co₃O₄ to CoO occurs. It is noticeable from the TGA recorded on Ni₇Co₃/C and Ni₁Co₉/C (Fig. 2b and c) that this last transformation of Co₃O₄ into CoO occurs at lower temperature than in the case of Co/C catalyst (Fig. 2d), between 700 °C and 900 °C, depending on the nickel content, instead of more than 1000 °C. The typical behavior of the Ni_xCo_{10-x}/C catalysts during the TGA confirms the expected formation of nickel and cobalt hydroxides supported on carbon. Hence, the catalysts synthesized are actually Ni_xCo_{10-x}(OH)₂₀/C (0 ≤ x ≤ 10), but for the sake of clarity, they are named Ni_xCo_{10-x}/C.

The final product obtained at high temperatures at the end of TGA consists in a NiO and CoO mix, which allows the determination of the metal loading on carbon. These loadings are given in Table 1 as the ratio:

$$\text{loading (wt\%)} = \frac{\text{mass}_{\text{metal}}}{\text{mass}_{\text{metal}} + \text{mass}_{\text{carbon}}} \quad (7)$$

The oxygen and hydrogen atoms present in the catalysts are excluded from the calculation since the catalyst loading was calculated before the synthesis and was only based on the three elements introduced (Ni, Co and C). Globally, the metal loadings on carbon are close to the nominal value of 30 wt%.

The catalyst metal content was measured by atomic absorption after dissolution of the catalyst. The nickel and cobalt contents are given in Table 1 and are in good agreement with the nominal Ni/Co ratios. However, all catalysts are slightly Ni rich.

The TEM images for three selected catalysts are presented in Fig. 3 (Ni/C, Ni₇Co₃/C and Co/C). The TEM images obtained for the other Ni_xCo_{10-x}/C catalysts (not shown) resemble that obtained for Ni₇Co₃/C catalyst. At first, a low contrast between the Ni_xCo_{10-x} nanostructures and the carbon substrate is noticeable, which makes

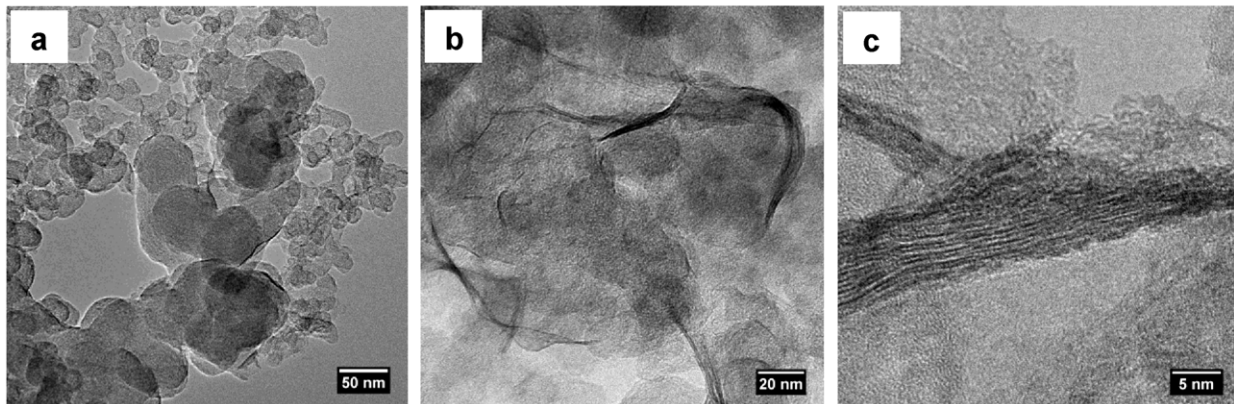
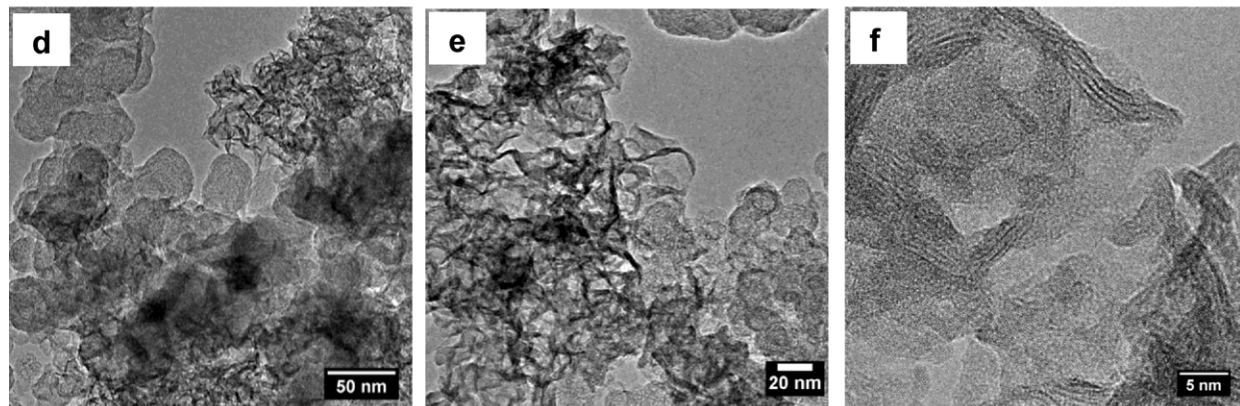
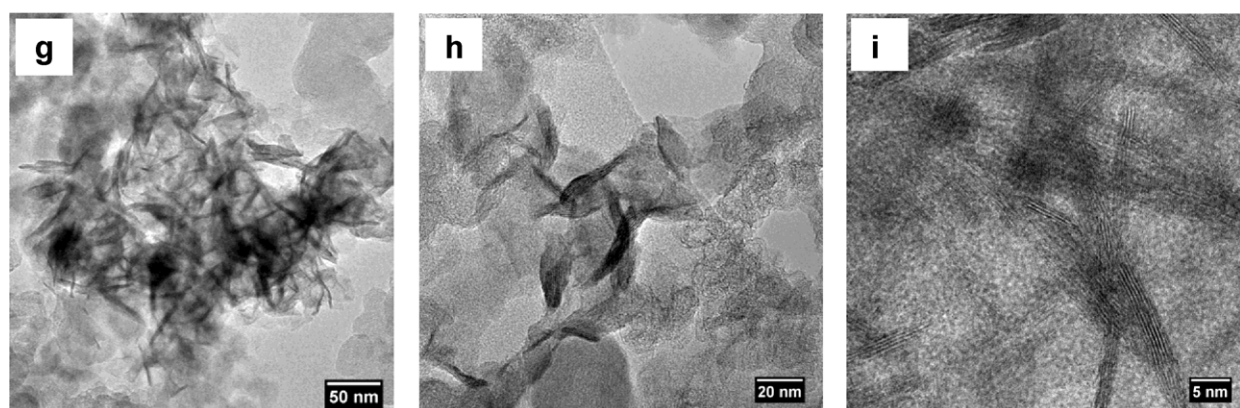
Ni / C**Ni₇Co₃ / C****Co / C**

Fig. 3. TEM images of (a), (b), (c) Ni/C catalyst, (d), (e), (f) Ni₇Co₃/C catalyst and (g), (h), (i) Co/C catalyst.

difficult the estimation of the average size of the catalyst. In TEM images given in Fig. 3a,d,g the Ni, Ni₇Co₃ and Co hydroxide structures give projections with size close to 50 nm (length and width); TEM image in Fig. 3c,f,i show 1-D projections which are interpreted as the cross section of planar structures. From the TEM images of the Ni/C catalyst, the nickel hydroxide nanostructures seem to wrap the carbon substrate (Fig. 3a–c), like nanoflakes deposited on carbon and following the shape of the substrate. For cobalt containing catalysts, this behavior is less pronounced (Fig. 3d–f for Ni₇Co₃/C and Fig. 3g–i for Co/C), and while these catalysts also present nanoflake shapes, they appear to be more rigid than Ni/C catalyst, with some needle-like structures appearing with a high contrast compared to carbon substrate. These needle-like structures were interpreted

as nanoflakes observed following one of their longer dimension, leading to a needle-like 2-D projection since flat nanostructures are also visible (Fig. 3d and 3g). Such nanoflake structure is commonly observed for Ni(OH)₂ and Co(OH)₂ materials [21,23,24], and resembles that of PdFe nanoleaves active for the oxygen reduction reaction reported by Zhang et al. [25].

The XRD patterns for Ni_xCo_{10-x}/C (Fig. 4) confirm the formation of β-Ni(OH)₂ and β-Co(OH)₂ structures [26,27] (JCPDS 14-0117 and 30-0443). The diffraction pattern was analyzed by the method of Levenberg–Marquardt, using a Voigt fit by means of a computer refinement program (Fityk free software [28]). The catalyst crystals are very small leading to a carbon (1 1 1) diffraction peak clearly visible with intensity comparable to that of nickel cobalt

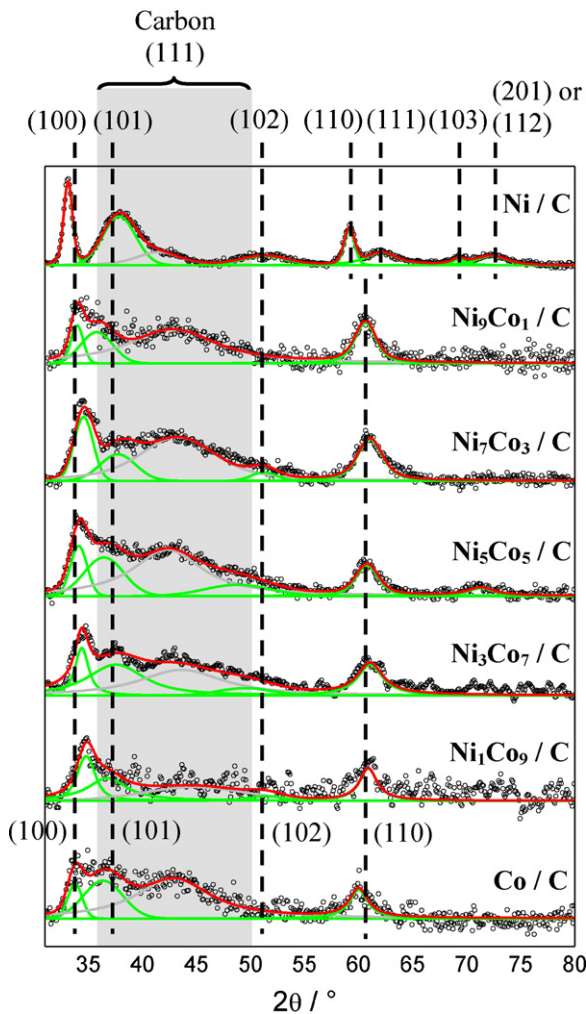


Fig. 4. XRD patterns recorded for $\text{Ni}_x\text{Co}_{10-x}/\text{C}$ catalysts. The more intense diffraction peaks are indexed with the corresponding planes. The green lines are the Voigt functions used to fit each diffraction peak; the red line is the fit of the whole diffraction pattern.

hydroxides. This low crystallinity of nickel cobalt hydroxides makes very difficult the accurate determination of the diffraction peak positions. However, a clear trend appears with a positive shift of the diffraction peaks from pure Co/C to $\text{Ni}_9\text{Co}_1/\text{C}$, indicating the probable formation of nickel cobalt alloy hydroxides. Furthermore, the hydroxide diffraction peaks present different widths depending on the crystallographic planes involved, with low relative intensity and a clear broadening of diffraction peaks corresponding to the (101), (102) and (111) planes when compared to the diffraction peaks related to (100) and (110) planes. The XRD data are hence confirming the TEM observation of the formation of flat structures, with a preferential growth along the (100) and (010) directions.

3.2. Electrochemical behavior

The voltammograms of $\text{Ni}_x\text{Co}_{10-x}/\text{C}$ catalysts recorded in 0.1 M NaOH supporting electrolyte in the range 0.05 V–1.55 V are presented in Fig. 5. These voltammograms correspond to stable ones obtained, after ten voltammetric cycles. The ten first voltammograms recorded to obtain a stable signal are presented in supporting informations (Figure S1). In this potential domain, the increase of cobalt content in the catalyst leads to a decrease of the catalyst stability. This low stability is characterized in Figure S1 by an initial irreversibility of the redox behavior of the catalyst with

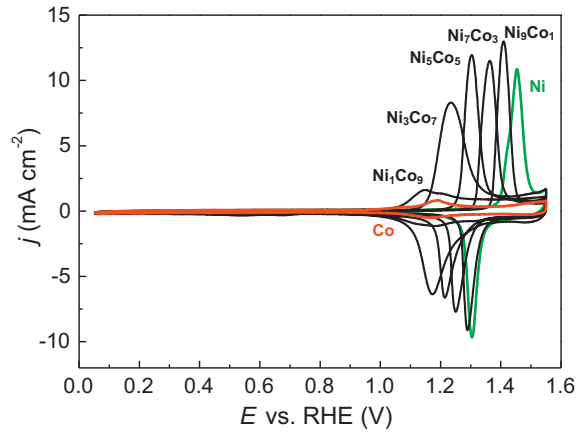


Fig. 5. voltammograms recorded for $\text{Ni}_x\text{Co}_{10-x}/\text{C}$ catalysts in 0.1 M NaOH electrolyte (scan rate: 10 mV s⁻¹, $T=25^\circ\text{C}$).

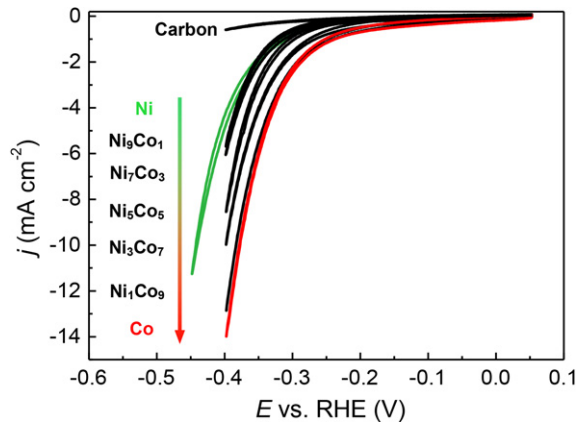
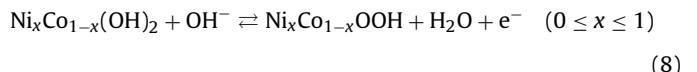


Fig. 6. voltammetry measurement in the HER potential domain for $\text{Ni}_x\text{Co}_{10-x}/\text{C}$ catalysts in 0.1 M NaOH electrolyte (scan rate: 10 mV s⁻¹, $T=25^\circ\text{C}$).

a higher charge involved in the anodic current peak than in the corresponding cathodic current peak, and a decrease of the current from the first to the tenth voltammetric cycle. The currents measured in the potential domain from 1.1 V to 1.5 V are relative to the oxidation of nickel cobalt hydroxides into oxy-hydroxides during the positive going scan and to the corresponding reduction reaction during the negative going scan according to equations (8):



A broadening and a negative shift of the current peak associated to this reaction occur when the cobalt content in the catalyst increases. This progressive change of the voltammogram shape with the catalyst composition indicates an interaction between nickel and cobalt which is consistent with the formation of alloys instead of separated $\text{Ni}(\text{OH})_2$ and $\text{Co}(\text{OH})_2$ phases.

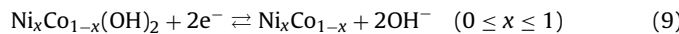
The voltammograms recorded in NaOH in the hydrogen evolution potential domain (from 0.05 V to -0.45 V) are presented in Fig. 6. The onset potential of the HER is comparable on the different $\text{Ni}_x\text{Co}_{10-x}/\text{C}$ catalysts (between -0.3 V and -0.2 V) while the water reduction current increases with the increase of cobalt content. This regular increase indicates the absence of a synergistic effect which could have occurred with the alloying of nickel and cobalt. Hence, the most active catalyst for the HER is Co/C . The comparison of the Tafel plots for the HER on $\text{Ni}_x\text{Co}_{10-x}/\text{C}$ (Fig. 7) reveals the same behavior for all catalysts with a first Tafel slope close to -240 mV decade⁻¹ in the low overpotential domain and a second one close to -120 mV decade⁻¹ at high overpotential region. Both Tafel slopes

Table 2

kinetic parameters determined for the HER on $\text{Ni}_x\text{Co}_{10-x}/\text{C}$ catalysts in 0.1 M NaOH.

Catalyst	Tafel slope (mV decade $^{-1}$)	j_0 (mA cm $^{-2}$)	α
Ni/C	−113	$8.75 \cdot 10^{-4}$	0.52
$\text{Ni}_9\text{Co}_1/\text{C}$	−104	$8.83 \cdot 10^{-4}$	0.57
$\text{Ni}_7\text{Co}_3/\text{C}$	−107	$1.14 \cdot 10^{-3}$	0.55
$\text{Ni}_5\text{Co}_5/\text{C}$	−109	$1.96 \cdot 10^{-3}$	0.54
$\text{Ni}_3\text{Co}_7/\text{C}$	−123	$5.68 \cdot 10^{-3}$	0.48
$\text{Ni}_1\text{Co}_9/\text{C}$	−126	$9.10 \cdot 10^{-3}$	0.47
Co/C	−128	$1.10 \cdot 10^{-2}$	0.46

are classically observed for the HER [29,30] and associated with a Volmer–Heyrovsky–Tafel kinetic mechanism. The kinetic data for the high overvoltage region are reported in Table 2 and are consistent with an increase of the catalytic activity of $\text{Ni}_x\text{Co}_{10-x}/\text{C}$ with the increase of cobalt content, with an exchange current density (j_0) increasing from ca. 10^{-3} mA cm $^{-2}$ for Ni/C to ca. 10^{-2} mA cm $^{-2}$ for Co/C. Another important observation can be made from the voltammograms recorded in the potential domain from 0.05 V to −0.4 V: the current peak corresponding to the reduction of $\text{Ni}_x\text{Co}_{10-x}(\text{OH})_2$ into $\text{Ni}_x\text{Co}_{10-x}$ [31,32] (Eq. (9)) is absent.



Cyclic voltammetry experiments were performed in the potential domain from −0.4 V to 1.55 V (not shown) with removal of hydrogen gas formed at the electrode between −0.4 V and −0.2 V in order to avoid the hydrogen oxidation current on $\text{Ni}_x\text{Co}_{10-x}/\text{C}$.

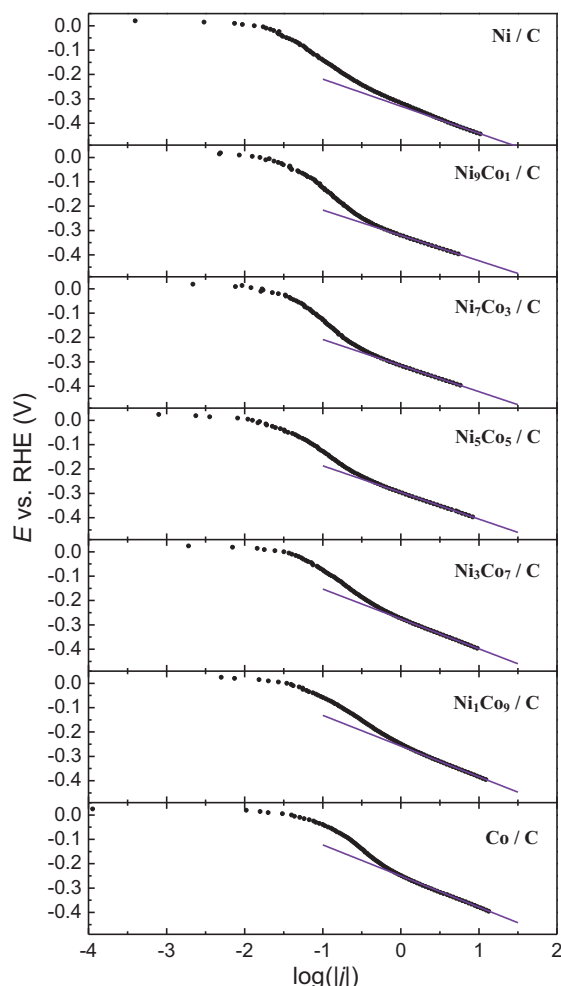


Fig. 7. Tafel plots of the HER on $\text{Ni}_x\text{Co}_{10-x}/\text{C}$ catalysts in 0.1 M NaOH electrolyte ($T=25^\circ\text{C}$). The purple line represents the $-120\text{ mV decade}^{-1}$ Tafel slope.

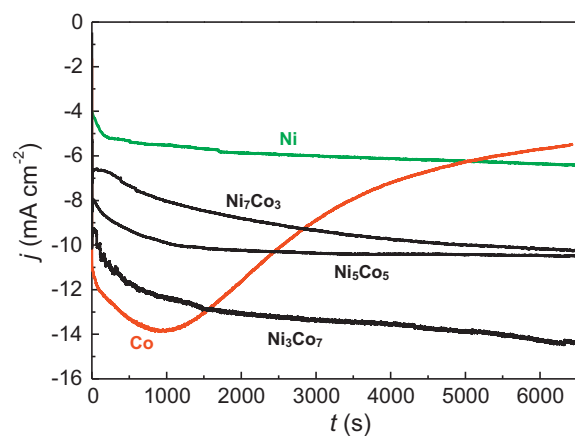


Fig. 8. chronoamperograms recorded during HER at -0.4 V vs. RHE on $\text{Ni}_x\text{Co}_{10-x}/\text{C}$ catalysts in 0.1 M NaOH electrolyte ($T=25^\circ\text{C}$).

[33]. These cycles were performed with different lower and upper potential limits. It was not possible to observe the faradic current corresponding to Eq. (9) for any of the $\text{Ni}_x\text{Co}_{10-x}/\text{C}$ catalysts. Furthermore, while scanning the whole potential range (from -0.4 V up to 1.55 V), the increase of the potential up to 1.55 V does not lead to the occurrence of an oxidation peak corresponding to the oxidation of a $\text{Ni}_x\text{Co}_{10-x}$ metal phase while the oxidation current of hydroxide into oxy-hydroxide is present. From these observations, it was not possible to identify the $\text{Ni}_x\text{Co}_{10-x}$ phase (metal or hydroxide) involved in the catalysis of HER.

The short term stability of $\text{Ni}_x\text{Co}_{10-x}/\text{C}$ catalysts during the HER was measured by chronoamperometry at -0.4 V . The resulting chronoamperograms are presented in Fig. 8. For all catalysts, on the beginning of the experiment, an activation process is observable with an increase of the absolute value of the HER current. In the case of Co/C, this activation process is followed by a decrease of the absolute value of the HER current indicating a drastic loss of activity associated with a low stability of the catalyst. This loss of activity is accompanied by a coloration of the electrolyte, also clearly observable in the case of $\text{Ni}_3\text{Co}_7/\text{C}$ catalyst, while no decrease of its activity was observed from the chronoamperometry curve. The analysis of electrolytes by atomic absorption revealed the presence of cobalt and the absence of nickel which is consistent with the increase of the electrolyte coloration with the increase of cobalt content, as observed by UV visible spectroscopy (Fig. 9). The

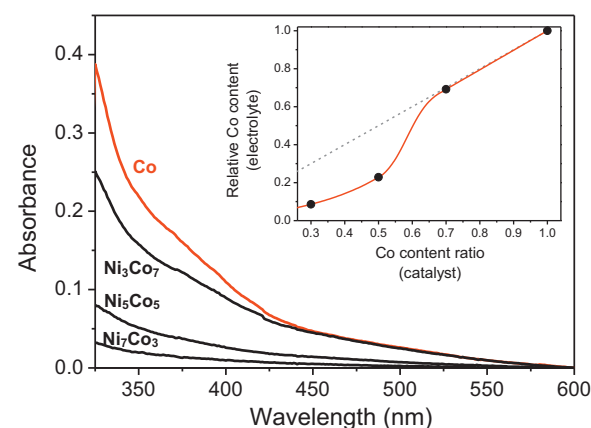


Fig. 9. UV-vis spectra recorded on 0.1 M NaOH electrolytes after the chronoamperometry measurements presented in Fig. 8. Inset: plot of the cobalt content in the electrolyte after the chronoamperometry at -0.4 V as a function of the cobalt content in the $\text{Ni}_x\text{Co}_{10-x}/\text{C}$ catalyst. The cobalt content in the electrolyte normalized at 1 for Co/C catalyst.

dissolution of cobalt, which forms, after precipitation, a suspension of small particles in the electrolyte leading to a pale brown coloration of the electrolyte, is difficult to explain in this low potential region. The hypothesis made to explain this selective cobalt dissolution, in the case where $\text{Ni}_x\text{Co}_{10-x}$ are under their hydroxide form, is the formation of $\text{Co}(\text{OH})_4^{2-}$ ions [34]. Indeed, the HER leads to the formation of hydrogen associated with an increase of the local pH at the vicinity of the electrode due to the formation of OH^- ions Eq. (2). The subsequent diffusion of $\text{Co}(\text{OH})_4^{2-}$ ions formed in the vicinity of $\text{Ni}_x\text{Co}_{10-x}/\text{C}$ electrode into the bulk 0.1 M NaOH electrolyte then leads to the precipitation of $\text{Co}(\text{OH})_2$ particles. However, the formation of $\text{Ni}(\text{OH})_4^{2-}$ from $\text{Ni}(\text{OH})_2$ is also reported [35], and this hypothesis could only partially explain a selective dissolution of cobalt from $\text{Ni}_x\text{Co}_{10-x}$ hydroxides.

From the UV visible analysis of the electrolytes, it was possible to determine the variation of cobalt amount in the solution and to compare it with the cobalt content ratio in the $\text{Ni}_x\text{Co}_{10-x}$ catalysts (inset in Fig. 9). The dashed line with a slope of 1 corresponds to the calculated Co content in the electrolyte versus the Co content in $\text{Ni}_x\text{Co}_{10-x}$ catalysts assuming that the dissolution of cobalt is unaffected by the presence of nickel. It appears that for $\text{Ni}_x\text{Co}_{10-x}$ catalysts with $7 \leq x \leq 10$, the presence of nickel doesn't change the cobalt dissolution rate. However, for $x \leq 5$, the dissolution rate of cobalt is drastically decreased, indicating a stabilization of the catalyst induced by the presence of nickel. This result is confirmed by atomic absorption analysis of the solution obtained after complete dissolution of the metal remaining on the electrode (results given in Table 1). A considerable decrease of the cobalt content in cobalt rich catalysts can be observed while the composition of the nickel rich catalyst (Ni_7Co_3) remains close to that measured for the freshly prepared catalyst.

4. Conclusion

The synthesis of $\text{Ni}_x\text{Co}_{10-x}/\text{C}$ catalysts led to the formation of $\text{Ni}_x\text{Co}_{10-x}$ nanoflakes dispersed on carbon (30 wt% metal on carbon) with a preferential growth of $\text{Ni}_x\text{Co}_{10-x}$ hydroxide crystals along the (1 0 0) and (0 1 0) directions. The electrochemical behavior of these materials in supporting electrolyte indicated a strong interaction between nickel and cobalt, and possibly, the formation of alloys. Their activity for HER increases with the increase of Co content, with an onset potential close to -0.2 V for Co/C catalyst and an exchange current density close to 10^{-2} mA cm^{-2} . However, due to the absence of the classically observed reduction current corresponding to the formation of metallic nickel and cobalt, the exact nature of the $\text{Ni}_x\text{Co}_{10-x}$ phase involved in the HER could not be clearly identified. Furthermore, the cobalt presented a poor stability during the HER for $x < 5$, while, for $x > 5$, an improvement of the cobalt stability due to the presence nickel could be obtained. Hence, the $\text{Ni}_5\text{Co}_5/\text{C}$ and $\text{Ni}_7\text{Co}_3/\text{C}$ catalysts present a good compromise between catalytic activity and stability, making them suitable cathode materials in an alcohol electrolysis cell at low current density. Indeed, such catalysts have the characteristics expected in terms

of catalytic activity, stability and cost for the preparation of high surface electrodes for the production of hydrogen and value added chemicals from alcohols.

Appendix A. Supplementary data

Supplementary data associated with this article can be found, in the online version, at <http://dx.doi.org/10.1016/j.apcatb.2013.01.051>.

References

- [1] B. Sørensen, Hydrogen and Fuel Cell Emerging Technologies and Applications, Elsevier Academic Press, New York, 2005.
- [2] V. Bambagioni, M. Bevilacqua, C. Bianchini, J. Filippi, A. Lavacchi, A. Marchionni, F. Vizza, P.K. Shen, *ChemSusChem* 3 (2010) 851–855.
- [3] A. Caravaca, F.M. Sapountzi, A. de Lucas-Consuegra, C. Molina-Mora, F. Dorado, J.L. Valverde, *International Journal of Hydrogen Energy* 37 (2012) 9504–9513.
- [4] C. Lamy, A. Lima, V. LeRhun, F. Delime, C. Coutanceau, J.-M. Léger, *Journal of Power Sources* 105 (2002) 283–296.
- [5] Y. Gu, F. Jérôme, *Green Chemistry* 12 (2010) 1127.
- [6] M. Simões, S. Baranton, C. Coutanceau, *ChemSusChem* 5 (2012) 2106.
- [7] M. Simões, S. Baranton, C. Coutanceau, *Applied Catalysis B* 110 (2011) 40.
- [8] D. Liang, J. Gao, J. Wang, P. Chen, Y. Wei, Z. Hou, *Catalysis Communications* 12 (2011) 1059.
- [9] M. Simões, S. Baranton, C. Coutanceau, *Applied Catalysis B* 93 (2010) 354.
- [10] M. Mougenot, A. Caillard, M. Simões, S. Baranton, C. Coutanceau, P. Brault, *Applied Catalysis B* 107 (2011) 372.
- [11] Claudio Bianchini, P.K. Shen, *Chemical Reviews* 109 (2009) 4183.
- [12] A. Ilie, M. Simões, S. Baranton, C. Coutanceau, S. Martemianov, *Journal of Power Sources* 196 (2011) 4965.
- [13] Z. Zhang, L. Xin, W. Li, *Applied Catalysis B* 119–120 (2012) 40.
- [14] C. Lamy, A. Devadas, M. Simões, C. Coutanceau, *Electrochimica Acta* 60 (2012) 112.
- [15] J.-M. Léger, S. Rousseau, C. Coutanceau, F. Hahn, C. Lamy, *Electrochimica Acta* 50 (2005) 5118.
- [16] M. Savy, *Electrochimica Acta* 13 (1968) 1359.
- [17] C.A. Marozzi, A.C. Chialvo, *Electrochimica Acta* 46 (2001) 861.
- [18] R.N. Singh, J.-F. Koenig, G. Poillerat, P. Chartier, *Journal of Electroanalytical Chemistry* 314 (1991) 241.
- [19] F. Gloaguen, N. Andolfatto, R. Durand, P. Ozil, *Journal of Applied Electrochemistry* 24 (1994) 863.
- [20] H. Hiano, E. Iguchi, H. Uschida, M. Watanabe, *Journal of Physical Chemistry B* 110 (2006) 16544.
- [21] Z. Liu, R. Ma, M. Osada, K. Takada, T. Sasaki, *Journal of the American Chemical Society* 127 (2005) 13869.
- [22] F. Bardé, M.-R. Palacín, B. Beaudoin, A. Delahaye-Vidal, J.-M. Tarascon, *Chemistry of Materials* 16 (2004) 299.
- [23] Z.X. Liu, Z.P. Li, H.Y. Qin, B.H. Liu, *Journal of Power Sources* 196 (2011) 4972.
- [24] X.L. Li, J.F. Liu, Y.D. Li, *Materials Chemistry and Physics* 80 (2003) 222.
- [25] Z. Zhang, K.L. More, K. Sun, Z. Wu, W. Li, *Chemistry of Materials* 23 (2011) 1570.
- [26] X. He, J. Li, H. Cheng, C. Jiang, C. Wan, *Journal of Power Sources* 152 (2005) 285.
- [27] L. Su, L. Gong, J. Gao, *Journal of Power Sources* 209 (2012) 141.
- [28] M. Wojdyl, *Journal of Applied Crystallography* 43 (2010) 1126.
- [29] M.R. Gennaro de Chialvo, A.C. Chialvo, *Journal of Electroanalytical Chemistry* 448 (1998) 87.
- [30] N. Krstajić, M. Popović, B. Grgur, M. Vojnović, D. Šepa, *Journal of Electroanalytical Chemistry* 512 (2001) 16.
- [31] P. Elumalaia, H.N. Vasana, N. Munichandraiah, *Journal of Power Sources* 93 (2001) 201.
- [32] D. Floner, C. Lamy, J.M. Léger, *Surface Science* 234 (1990) 87.
- [33] S. Maximovitch, R. Durand, *Journal of Electroanalytical Chemistry* 149 (1983) 273.
- [34] N.V. Plyasunova, Y. Zhang, M. Muhammed, *Hydrometallurgy* 48 (1998) 153.
- [35] N.V. Plyasunova, Y. Zhang, M. Muhammed, *Hydrometallurgy* 48 (1998) 43.